Chinese Chemical Letters 33 (2022) 2915–2918

Contents lists available at ScienceDirect

Chinese Chemical Letters

journal homepage: www.elsevier.com/locate/cclet

Anchoring metal ions in amine-functionalized boron imidazolate framework for photocatalytic reduction of CO_2

Guilan Xu[a], Qin-Long Hong[a], Yayong Sun[a], Meng Liu[b], Hai-Xia Zhang[a,*], Jian Zhang[a,*]

[a] State Key Laboratory of Structural Chemistry, Fujian Institute of Research on the Structure of Matter, Chinese Academy of Sciences, Fuzhou 350002, China
[b] Key Lab for Sport Shoes Upper Materials of Fujian Province, Fujian Huafeng New Material Co., Ltd., Putian 351164, China

ARTICLE INFO

Article history:
Received 6 September 2021
Revised 8 October 2021
Accepted 21 October 2021
Available online 27 October 2021

Keywords:
Metal-organic framework
CO_2 reduction
Boron-imidazolate framework
Photocatalysis
Structure

ABSTRACT

The photocatalytic reduction of CO_2 to energy-rich chemicals is highly appealing for alleviation of energy crisis and environment pollution. The introduction of different active sites is a key factor to determine the reaction activity and selectivity. Here, we demonstrate the metal ion-dependent performance for photocatalytic CO_2 reduction by anchoring transition metal ions (Co^{2+} and Ni^{2+}) in an amine-functionalized boron imidazolate framework (**BIF-43**). As a result, Ni@**BIF-43** realized a high selectivity of 90.2% for the CO_2-to-CO, while Co@**BIF-43** achieved more efficient conversion with a high CO production rate of 2036.0 μmol g^{-1} h^{-1}. Significantly, precise control of isolated metal site on a well-defined structure through coordination-assisted strategies enables us to better understand the specific effects of different metal-ion species on photoreduction of CO_2 as well as the catalytic mechanism.

Excessive emission of carbon dioxide (CO_2) from the burning fossil fuels results in serious global climatic change and energy shortage [1–4]. Currently, the photocatalytic conversion of CO_2 to valuable energy-rich chemicals has been considered as one of promising technologies to alleviate above issues [5–8]. Unfortunately, owing to the high thermodynamic stability of CO_2 molecule, the activation and reduction of CO_2 are very difficult and complex [9,10]. The multiple proton coupled electron transfer process is required to CO_2 photoreduction, which is accompanied by the competing hydrogen evolution reduction (HER) leading to a wide variety of products [11]. In the past several decades, a series of efficient photocatalysts based on semiconductors (such as TiO_2, CdS, g-C_3N_4) and nanocomposites have been developed [12–22]. Due to the complicated structural components of catalysts and the large number of possible products, fundamental understanding the dependence between the structure and composition of catalyst on the activity and selectivity of CO_2 photoreduction is a significant challenge.

Loading active metal atoms/ions onto heterogeneous supports is a very versatile route to maximize the fraction of active sites and tailor properties of catalysts [23,24]. The transition-metal (TM) catalyst has attracted worldwide attention in catalytic field. Especially, the metal Ni and Co serving as active sites play important roles in catalytic reaction [5,7,13,19]. Generally, active carbon, metal oxides, silica and zeolites are the most common supports, because of their effective voids and defect sites [25–31]. However, it is difficult to precisely control the location and the local environment of metal atoms/ions on these mostly disordered anchoring surfaces, easily resulting in nonuniform distribution as well as complicated metal–support interactions. Compared with the conventional inorganic supports, metal-organic frameworks (MOFs) possess many attractive features such as well-defined structure, high surface area, tunable inorganic nodes and organic linkers, and rich surface coordination sites, and have thus emerged as possible supporters to embed catalytic metal sites [32–36]. Introducing TM atoms into a MOF matrix could open up great opportunities to tune the electronic properties of TMs as CO_2RR active sites and maintain relatively simple atomic coordination for fundamental mechanism study. Recently, many studies have shown that MOFs can serve as functional supports for anchoring external metal sites on secondary building units (SBU) or organic struts [37–41]. However, the reaction condition for photocatalytic reduction of CO_2 is somewhat harsh, and it is urgently needed to develop new porous and stable functional MOFs.

Boron imidazolate frameworks (BIFs), a kind of MOFs constructed by the crosslinking of pre-synthesized boron imidazolate ligands and metal ions, are unexpectedly found to show improved chemical stability due to the presence of robust M-N coordination bonds and the strong covalent B-N bonds [42]. Recently, some BIFs have been used as catalysts to reduction CO_2 study, which offered

* Corresponding authors.
E-mail addresses: zhanghaixia@fjirsm.ac.cn (H.-X. Zhang), zhj@fjirsm.ac.cn (J. Zhang).

https://doi.org/10.1016/j.cclet.2021.10.061
1001-8417/

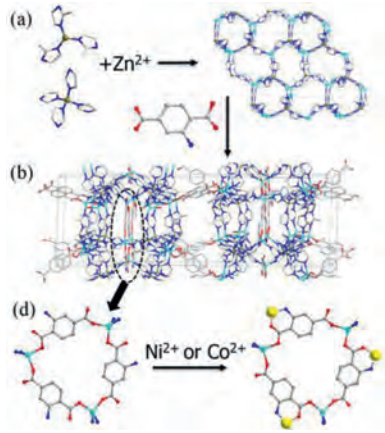

Fig. 1. Structural analysis of **BIF-43**. (a) The 2D boron imidazolate layer linked by $BH(mim)_3^-$, $B(im)_4^-$ and metal ions. (b) 3D structure of **BIF-43**. (c) Details of the $Zn_3(2\text{-ATP})_3$ ring.

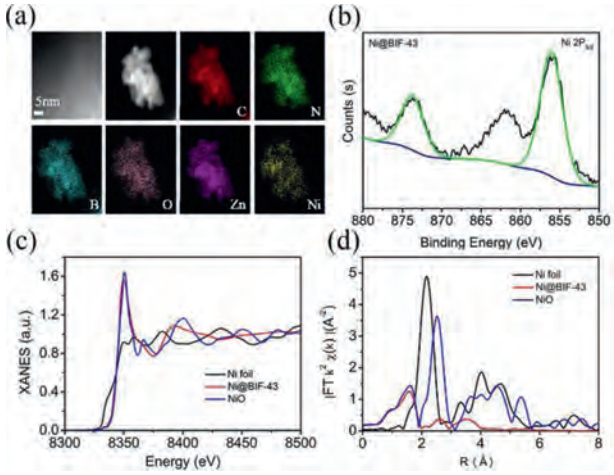

Fig. 2. (a) HRTEM images and element mapping of Ni**@BIF-43**. (b) The high resolution XPS spectrum of Ni 2p for Ni**@BIF-43**. (c) XANES spectra of Ni**@BIF-43** for Ni K-edge. (d) Fourier transformed (FT) k^2-weighted χ(k)-function of the EXAFS spectra for Ni K-edge.

accurate insight into the catalytic processes *via* adjusting the local environment of metal nodes [43–47]. However, it is difficult to anchor metal on the organic struts in BIFs because of the lack of uncoordinated functional groups, such as −COOH, −OH, $-NH_2$. Consequently, the construction of BIF-based catalyst with a special binding microenvironment to provide a new direction to functionalize BIFs is quite desirable.

Here, we designed an amine-functionalized boron imidazolate framework (**BIF-43**) which was used as a support to stabilize the transition metal ions ($Ni^{2+}$and Co^{2+}) in pores, obtaining Ni**@BIF-43** and Co**@BIF-43**. By anchoring external metal ions, it offered a simple and precise structural model to analyze the metal nodes-dependent effect on photoreduction of CO_2. As expected, the **BIF-43** with different catalytic active centers exhibit diverse effects on the activity and selectivity of mainly reductive products. It is worth noting that Ni**@BIF-43** showed very high catalytic selectivity (90.2%) for CO, which has far exceeded the selectivity of Co**@BIF-43** (64.1%). The close contact between adsorption sites and active sites effectively activates CO_2 molecules and improves photocatalytic conversion of CO_2. This strategy offered us an important insight to prepare BIF-based materials for CO_2 capture and photoreduction.

BIF-43 ($Zn_{11}[B(im)_4]_6[BH(mim)_3]_2(2\text{-ATP})_6(OH)_2$, im = imidazole, mim = 2-methylimidazole, 2-ATP = 2-aminoterephthalic acid) was successfully designed and synthesized through the self-assembly of $Zn(CH_3COO)_2{\cdot}2H_2O$ and three different ligands $KBH(2\text{-mim})_3$, $KB(im)_4$ and 2-ATP (summary of crystal data and structural refinements are shown in Table S1 in Supporting information). It is the first example that integrates both tetradentate $B(im)_4^-$ ligand and tridentate $BH(mim)_3^-$ ligand. Despite such a complex composition, **BIF-43** can be simply considered to be built from the 2D boron-imidazolate-zinc layer pillared by the 2-ATP ligands. The single-crystal X-ray diffraction analysis exhibits that **BIF-43** crystallizes in the hexagonal space group *P*62c and features a 3D pore structure. There are three crystallographically independent tetrahedral zinc sites in the asymmetric unit. Each Zn1 is bonded to three N from two $B(im)_4^-$ and one $BH(mim)_3^-$, and one O atoms from 2-ATP ligand (Fig. S1 in Supporting information). Each Zn2 is bonded to three N from three $B(im)_4^-$ and one charge-balancing OH^- (Fig. S2 in Supporting information). Zn1 and Zn2 ions are bridged by $B(im)_4^-$ and $BH(mim)_3^-$ ligands to form a *hcb* layer parallel to the *ab* plane (Fig. 1a). Two such layers are bridged by Zn3 ions to form a 2D sandwich-like layer, with $Zn_3(2\text{-ATP})_3$ rings at the center of the sandwich layer (Figs. 1b and c and Fig. S3 in Supporting information). Furthermore, these sandwich layers are linked by 2-ATP ligands that bonded on Zn1 to yield a 3D porous structure (Fig. 1b). Its phase purity, thermal and chemical stability were confirmed by powder X-ray diffraction (PXRD) and thermogravimetry analysis (TGA) (Figs. S4-S7 in Supporting information). As estimated by the PLATON program, the free space in **BIF-43** is 5459.2 $Å^3$ per unit cell with the pore volume ration of 43.0%. N_2 sorption measurements (Fig. S8 in Supporting information) at 77 K exhibit type-I isotherms behavior with the calculated Brunauer-Emmett-Teller (BET) and Langmuir surface areas of 539.8 and 779.3 m^2/g, respectively. Moreover, **BIF-43** shows a high affinity for CO_2 due to the presence of $-NH_2$ in the pore [48,49]. The CO_2 uptake values are 97.2 cm^3/g at 273 K and 63.9 cm^3/g at 298 K under 1 atm (Fig. S9 in Supporting information). The adsorption enthalpy (Q_{st}) near the zero coverage was calculated to be 32.4 kJ/mol, which was significantly higher than those reported BIFs without $-NH_2$ groups [50]. The stronger affinity of **BIF-43** toward CO_2 is more conductive to the activation of CO_2 during the reduction process.

Owing to the presence of 2-ATP in the pore wall, the adjacent free -NH_2 and uncoordinated O-atoms of the 2-ATP could be used to chelate external metal ions in the pores of **BIF-43** (Fig. 1c) [51–53]. Therefore, the metalated compounds Ni**@BIF-43** were created by immersing the pristine crystals in solutions of Ni^{2+} under air at room temperature. The color of the crystals changed from pale yellow to light green suggesting the adsorption of external metal ions (Fig. S11 in Supporting information). The PXRD (Fig. S12 in Supporting information) demonstrated the retention of **BIF-43** crystallinity after loading of Ni ions. Ni**@BIF-43** remained porous and showed reduced porosity as demonstrated by N_2 sorption isotherms (Fig. S8). The BET surface was decreased from 539.8 m^2/g for BIF-43 to 275.1 m^2/g for Ni**@BIF-43**. The coordination of Ni ions with the $-NH_2$/O groups of **BIF-43** was further confirmed by Fourier transform infrared (FT-IR) spectra. As shown in Fig. S13 (Supporting information), the peaks at 1612 and 1450 cm^{-1} for Ni**@BIF-43** displayed a significantly lower intensity compared to that for **BIF-43**, which are ascribed to the $-NH_2$ and −COO stretch vibrations, strongly supporting the interaction between Ni ions and $-NH_2$/O species [54]. Inductively coupled plasma atomic emission spectroscopy (ICP-AES) showed that the Ni^{2+} content was 2.1%. The high resolution transmission electron microscopy (HRTEM) images clearly confirmed that no Ni nanoparticles and metal oxides are formed during the immersion period, shown in Fig. 2a. Element mapping revealed uniform distribution of Ni ions throughout entire **BIF-43** crystal. To gain further structural details on the chemical status and elemental composition of the samples, we performed X-ray photoelectron spec-

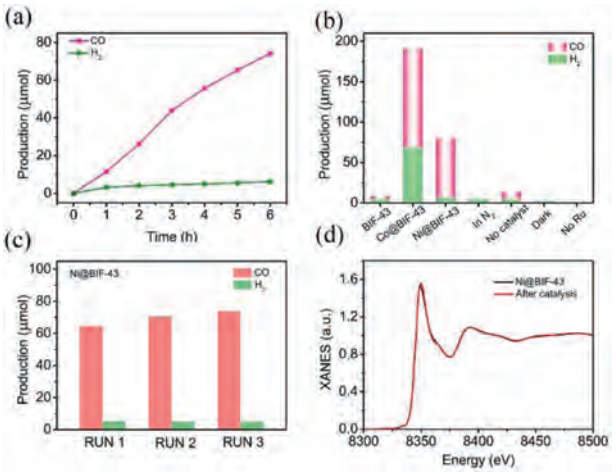

Fig. 3. (a) Time course of CO and H_2 evolution over Ni@**BIF-43**. (b) The evolution yield of CO and H_2 at different condition. (c) The reproducible photocatalytic activities for Ni@**BIF-43**. (d) EXAFS of Ni@**BIF-43** before and after the photocatalytic CO_2 reduction.

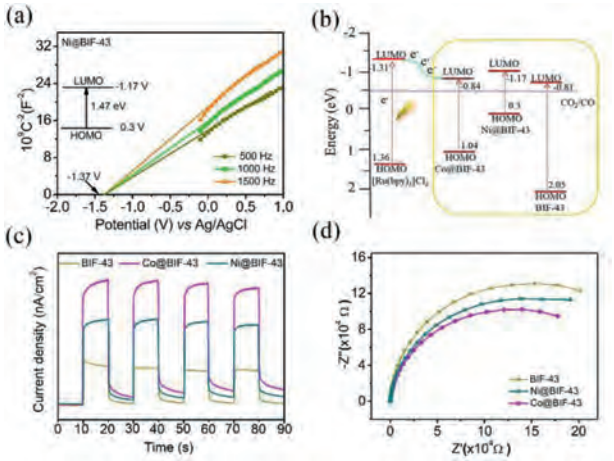

Fig. 4. (a) Mott–Schottky plots for Ni@**BIF-43** in 0.2 mol/L Na_2SO_4 aqueous solution. (b) Schematic energy-level diagram showing electron transfer from $[Ru(bpy)_3]Cl_2$ to the **BIF-43**, Co@**BIF-43** and Ni@**BIF-43**. (c) Transient photocurrent response for **BIF-43**, Co@**BIF-43** and Ni@**BIF-43** under visible light ($420 < \lambda < 800$ nm). (d) Electrochemical impedance spectroscopy plots for **BIF-43**, Co@**BIF-43** and Ni@**BIF-43** under visible light ($420 < \lambda < 800$ nm).

troscopy (XPS) and X-ray absorption spectroscopy (XAS) measurements. The XPS survey scan clearly showed the presence of C, N, O, B, Zn, Ni in Ni@**BIF-43** (Fig. S14 in Supporting information). As shown in Fig. 2b, the binding energy of Ni 3p peak centered at 856.10 eV, which was assigned to Ni^{2+} [7]. The X-ray absorption near-edge structure (XANES) spectra (Fig. 2c) also showed that the absorption edge positions of Ni@**BIF-43** is also close to that of NiO, which coincided well with the XPS results. In addition, the Fourier-transformed (FT) extended X-ray absorption fine structure (EXAFS) analysis (Fig. 2d) in *R* space of Ni showed one main peak at 1.56 Å, which is longer than the distance of Ni-N (1.40 Å) and slightly shorter than that of Ni-O (1.59 Å), likely due to the Ni-O and Ni-N combined contributions. No Ni-Ni bonds at around 2.20 Å are observed. Altogether, these results underline the presence of Ni^{2+} ions in an atomically dispersed form, which is coordinated to the $-NH_2/O$ species of the 2-ATP ligands in **BIF-43**.

Photocatalytic CO_2 reduction reactions at room temperature have been investigated in CO_2-saturated CH_3CN/H_2O solution with triethanolamine (TEOA) as sacrificial reagent and $Ru(bpy)_3]Cl_2$ (noted Ru) as photosensitizer under visible light ($420 < \lambda < 800$ nm) irradiation [5,26,44,55]. In this reaction system, CO and H_2 were detected as the main reduction products and no appreciable amounts of other carbonous products were detected from the reaction (Fig. S15 in Supporting information). As shown in Fig. 3a, the yields of CO and H_2 increases almost linearly with irradiation time in a 6 h reaction. The total amounts of CO and H_2 products from Ni@**BIF-43** catalytic system were 66.5 b5~mol (rate: 1109.0 b5~mol g^{-1} h^{-1}) and 7.2 b5~mol (rate: 121.1 b5~mol g^{-1} h^{-1}), respectively, giving a high CO selectivity of 90.2%. The apparent quantum efficiency for CO production was measured to be 0.060% at 450 nm (Fig. S26 in Supporting information). It should be noted that the catalytic performance of pristine crystals **BIF-43** without anchoring external metal ions was rather poor and nearly undetectable. Therefore, these results demonstrated that the anchored metal ions serve as the catalytic sites for CO_2 photoreduction [51,52].

Control experiments were carried out to further understand the CO_2 reduction under different conditions and these results were shown in Fig. 3b. No products were detected in the absence of visible light or Ru, suggesting that the CO_2 reduction is indeed driven by the photoirradiation. When CO_2 was replaced by N_2, only H_2 can be detected while no CO is observed, implying that the CO derived from conversion of CO_2. In the absence of Ni@**BIF-43** catalysts, only trace amount of CO and H_2 were detected, which came from the Ru catalysts and were negligible as compared to that with Ni@**BIF-43** catalysts. These results confirmed that the CO_2 reduction reaction was indeed catalyzed by Ni@**BIF-43** and driven by light excitation of the Ru photosensitizer. Additionally, Ni@**BIF-43** exhibited high durability in cycling tests with reasonably reproducible photocatalytic activities for all three cycles, shown in Fig. 3c. XRD analysis (Fig. S16 in Supporting information) evidenced that the crystallinity of the catalysts is maintained. Moreover, XANES (Fig. 3d) and EXAFS (Fig. S17 in Supporting information) measurements of Ni have been examined after photocatalytic reaction. No obvious structural evolution has been observed, further reflecting its stability during the CO_2 photoreduction process.

The well functionalized porous platform of **BIF-43** allows us to investigate the significant role of different metal sites in CO_2 photocatalytic reaction. In comparison, Co with only one d-orbital electron less than Ni has been investigated to construct a counterpart sample of Co@**BIF-43**. The Co content was 0.52% as determined by ICP-AES analysis. HRTEM, element mapping, photograph and XPS analyses revealed that Co was uniformly distributed throughout the crystal in the form of Co^{2+} ions (Figs. S18-S20 in Supporting information). In the similar photocatalytic condition, Co@**BIF-43** displayed a higher photocatalytic activity (2036.0 b5~mol g^{-1} h^{-1} for CO) than that of Ni@**BIF-43** (1109.0 b5~mol g^{-1} h^{-1}), however, its selectivity (64.1%) was obviously lower than that of Ni@**BIF-43** (90.2%) (Fig. 3b and Fig. S21 in Supporting information). The apparent quantum efficiency for CO production was measured to be 0.061% at 450 nm (Fig. S27 in Supporting information). In addition, three cycles reactions experiments were conducted to evaluate the stability of the photocatalyst (Fig. S22 in Supporting information).

To elucidate the mechanisms behind the metal sites dependent performance for CO_2 photoreduction, we studied the whole reaction process systematically. Firstly, the electronic structure of catalyst is one key factor to determine the photocatalytic capability. The UV-vis diffuse reflectance spectra (Figs. S23 and S24 in Supporting information) were conducted to give the bandgap energy of 2.86, 1.88 and 1.47 eV for **BIF-43**, Co@**BIF-43** and Ni@**BIF-43**, respectively. Mott-Schottky measurements were carried out to determine the flat-band position to be −0.81, −0.84 and −1.17 eV for **BIF-43**, Co@**BIF-43** and Ni@**BIF-43** (Fig. 4a and Fig. S25 in Supporting information), respectively, which are approximately close to the bottom of the conduction band (CB). Combined with the analysis of the UV-vis diffuse reflectance spectra, the energy level diagrams

for all three catalysts are obtained (Fig. 4b). The CB potential for all the three catalysts were higher than the reduction potential of CO_2-to-CO and lower than the lowest unoccupied molecular orbital (LUMO) of Ru (−1.27 eV) [5]. These results suggested that these catalysts were thermodynamically capable of receiving the photoexcited electrons from the excited Ru for reducing the adsorbed CO_2 to CO product. However, although the catalytic activity of Co**@BIF-43** was higher than that of Ni**@BIF-43**, its CB potential was lower than that of Ni**@BIF-43**. Therefore, energy band positions only endow sufficient driving force to trigger the CO_2 reduction process but cannot determine the catalytic activity. Furthermore, charge separation efficiency of these catalysts was investigated by the transient photocurrent response and the electrochemical impedance spectroscopy (EIS) under the photocatalytic system condition, shown in Figs. 4c and d. Greatly enhanced photocurrent intensity and reduced semicircle arc of Nyquist plots have been observed over Co**@BIF-43** and Ni**@BIF-43**, suggesting the enhanced separation efficiency of the photogenerated electron-hole pairs and faster electron transfer from the excited Ru photosensitizer to the reaction center by anchoring Co/Ni ions. Based on previous works [5,37] and the above results, a conceivable mechanism was proposed. Under visible light irradiation, the photosensitizer (Ru) is promoted to the excited state. This excited state is then oxidatively quenched by the catalyst of M**@BIF-43** and transfers electron to the exposed metal active site where CO_2 molecule is activated and reduced to CO. Finally, Ru returned back to its original state by electron supply from the sacrificial reductant TEOA. Moreover, the highest current intensity and lowest charge-transfer resistance of Co**@BIF-43** was consistent with its highest catalytic activity towards CO, which demonstrates that charge separation and transport efficiency may be the key factor for the boosted catalytic reaction rate. Whereas, Ni**@BIF-43** shows the higher selectivity of CO over H_2, indicating the important selective role of the metal center in the catalytic process. The above results clearly indicate that BIFs modified by transition metal ions can significantly facilitate the charge separation, and vastly improve photocatalytic CO_2 efficiency, and the catalytic performances highly dependent the types of active metal ions.

In summary, an amine-functionalized **BIF-43** was reasonably designed and used as the supporter to stabilize active sites Co and Ni, thereby obtaining photocatalysts Ni**@BIF-43** and Co**@BIF-43**. Ni**@BIF-43** exhibited a high selectivity of 90% for the CO_2-to-CO conversion, while Co**@BIF-43** performed a high CO production rate of 2036.0 μmol g^{-1} h^{-1}. The close connection between active sites and adsorption sites, and the enhanced photo-excited electrons transfer together promoted photocatalytic CO_2 efficiency. Furthermore, the model allows us to realize more definitively the specific effects of different metal-ion species on CO_2 conversion. The work provided more insights into the design of photocatalysts by anchoring active sites *via* functional organic ligands as linker.

Declaration of competing interest

The authors declare no conflicts of interests.

Acknowledgments

This work is supported by National Natural Science Foundation of China (Nos. 21935010, 21773242), National Key Research and Development Program of China (No. 2018YFA0208600), and the Strategic Priority Research Program of the Chinese Academy of Sciences (No. XDB20000000).

Supplementary materials

Supplementary material associated with this article can be found, in the online version, at doi:10.1016/j.cclet.2021.10.061.

References

[1] J. Wu, Y. Huang, W. Ye, Y. Li, Adv. Sci. 4 (2017) 1700194.
[2] J. Ran, M. Jaroniec, S.Z. Qiao, Adv. Mater. 30 (2018) 1704649.
[3] J. Wu, X.D. Zhou, Chin. J. Catal. 37 (2016) 999–1015.
[4] J. Liu, C. Chen, K. Zhang, L. Zhang, Chin. Chem. Lett. 32 (2021) 649–659.
[5] X.K. Wang, J. Liu, L. Zhang, et al., ACS Catal. 9 (2019) 1726–1732.
[6] H.L. Wu, X.B. Li, C.H. Tung, L.Z. Wu, Adv. Mater. 31 (2019) 1900709.
[7] W. Zhong, R. Sa, L. Li, et al., J. Am. Chem. Soc. 141 (2019) 7615–7621.
[8] Z. Wu, S. Guo, L.H. Kong, et al., Chin. J. Catal. 42 (2021) 1790–1797.
[9] W. Tu, Y. Zhou, Z. Zou, Adv. Mater. 26 (2014) 4607–4626.
[10] F. Li, X. Yue, H. Zhou, J. Fan, Q. Xiang, Chin. J. Catal. 42 (2021) 1608–1616.
[11] R. Li, W. Zhang, K. Zhou, Adv. Mater. 30 (2018) 1705512.
[12] B. Sarkar, R. Goyal, L.N.S. Konathala, et al., Appl. Catal. B: Environ. 217 (2017) 637–649.
[13] M.F. Kuehnel, K.L. Orchard, K.E. Dalle, E. Reisne, J. Am. Chem. Soc. 139 (2017) 7217–7223.
[14] M. Ou, W. Tu, S. Yin, et al., Angew. Chem. Int. Ed. 57 (2018) 13570–13574.
[15] J.C. Wang, L. Zhang, W.X. Fang, et al., ACS Appl. Mater. Interfaces 7 (2015) 8631–8639.
[16] F.L. Zeng, H.L. Zhu, X.L. Chen, L.B. Qu, B. Yu, Green Chem. 23 (2021) 3677–3682.
[17] Q. Yang, G. Pan, J. Wei, et al., ACS Sustain. Chem. Eng. 9 (2021) 2367–2377.
[18] Y.F. Si, K. Sun, X.L. Chen, et al., Org. Lett. 22 (2020) 6960–6965.
[19] Y. Xia, J. Yu, Chem 6 (2020) 1039–1040.
[20] J. Fu, K. Jiang, X. Qiu, J. Yu, M. Liu, Mater. Today 32 (2020) 222–243.
[21] F. Xu, K. Meng, B. Cheng, et al., Nat. Commun. 11 (2020) 4613–4621.
[22] J. Low, B. Dai, T. Tong, C. Jiang, J. Yu, Adv. Mater. 31 (2019) 1802981.
[23] X. Wang, X. Zhang, R. Pandharkar, et al., ACS Catal. 10 (2020) 8995–9005.
[24] X. Fang, Q. Shang, Y. Wang, et al., Adv. Mater. 30 (2018) 1705112.
[25] W. Bi, X. Li, R. You, et al., Adv. Mater. 30 (2018) 1706617.
[26] Y. Wang, S. Wang, X.W.D. Lou, Angew. Chem. Int. Ed. 58 (2019) 17236–17240.
[27] G.R. Jenness, J.R. Schmidt, ACS Catal. 3 (2013) 2881–2890.
[28] D. Kim, N. Becknell, Y. Yu, P. Yang, Nano Lett. 17 (2017) 2732–2737.
[29] K. Okumura, S. Matsumoto, N. Nishiaki, M. Niwa, Appl. Catal. B: Environ. 40 (2003) 151–159.
[30] A.W. Petrov, D. Ferri, F. Krumeich, et al., Nat. Commun. 9 (2018) 2545–2552.
[31] N. Li, M. Huang, J. Zhou, M. Liu, D. Jing, Chin. J. Catal. 42 (2021) 781–794.
[32] D. Wang, R. Huang, W. Liu, D. Sun, Z. Li, ACS Catal. 4 (2014) 4254–4260.
[33] Y. Wang, N.Y. Huang, J.Q. Shen, et al., J. Am. Chem. Soc. 140 (2018) 38–41.
[34] B. Li, Z. Ju, M. Zhou, K. Su, D. Yuan, Angew. Chem. Int. Ed. 58 (2019) 7687–7691.
[35] Y.S. Wei, M. Zhang, R. Zou, Q. Xu, Chem. Rev. 120 (2020) 12089–12174.
[36] A.M. Abdel-Mageed, B. Rungtaweevoranit, M. Parlinska-Wojtan, et al., J. Am. Chem. Soc. 141 (2019) 5201–5210.
[37] J.D. Evans, C.J. Sumby, C.J. Doonan, Chem. Soc. Rev. 43 (2014) 5933–5951.
[38] X. Cui, J. Wang, B. Liu, et al., J. Am. Chem. Soc. 140 (2018) 16514–16520.
[39] L.Z. Dong, L. Zhang, J. Liu, et al., Angew. Chem. Int. Ed. 59 (2020) 2659–2663.
[40] J. Pang, Z. Di, J.S. Qin, et al., J. Am. Chem. Soc. 142 (2020) 15020–15026.
[41] Y. Guo, Y. Wang, Y. Shen, et al., J. Am. Chem. Soc. 142 (2020) 21493–21501.
[42] H.-X. Zhang, M. Liu, T. Wen, J. Zhang, Coord. Chem. Rev. 307 (2016) 255–266.
[43] T. Wen, M. Liu, S. Chen, et al., Small 16 (2020) 1907669.
[44] Q.-L. Hong, H.-X. Zhang, J. Zhang, J. Mater. Chem. A 7 (2019) 17272–17276.
[45] H.-X. Zhang, Q.-L. Hong, J. Li, et al., Angew. Chem. Int. Ed. 58 (2019) 11752–11756.
[46] P. Shao, W. Zhou, Q.-L. Hong, et al., Angew. Chem. Int. Ed. 60 (2021) 16687–16692.
[47] G. Xu, H. Zhang, J. Wei, et al., ACS Nano 12 (2018) 5333–5340.
[48] Y. Fu, D. Sun, Y. Chen, et al., Angew. Chem. Int. Ed. 51 (2012) 3364–3367.
[49] L. Xiang, L. Sheng, C. Wang, et al., Adv. Mater. 29 (2017) 1606999.
[50] H.X. Zhang, H.R. Fu, H.Y. Li, J. Zhang, X. Bu, Chem. Eur. J. 19 (2013) 11527–11530.
[51] X. Wang, W. Chen, L. Zhang, et al., J. Am. Chem. Soc. 139 (2017) 9419–9422.
[52] G. Wang, C.T. He, R. Huang, et al., J. Am. Chem. Soc. 142 (2020) 19339–19345.
[53] T. Wen, Y. Zheng, C. Xu, et al., Mater. Horiz. 5 (2018) 1151–1155.
[54] G.G. Chang, X.C. Ma, Y.X. Zhang, et al., Adv. Mater. 31 (2019) 1904969.
[55] K. Zhao, S. Zhao, C. Gao, et al., Small 14 (2018) 1800762.